

1 **Tropopause Evolution in a Rapidly Intensifying Tropical Cyclone: A Static**  
2 **Stability Budget Analysis in an Idealized, Axisymmetric Framework**

3 Patrick Duran\* and John Molinari

4 *University at Albany, State University of New York, Albany, NY*

5 \**Corresponding author address:* Department of Atmospheric and Environmental Sciences, Univer-  
6 sity at Albany, State University of New York, 1400 Washington Avenue, Albany, NY.

7 E-mail: pduran2008@gmail.com

## ABSTRACT

8 Large changes in tropopause-layer static stability are observed during the  
9 rapid intensification (RI) of an idealized, axisymmetric tropical cyclone (TC).  
10 Over the eye, static stability near the tropopause decreases and the cold-point  
11 tropopause height rises by up to 4 km at the storm center. Outside of the eye,  
12 static stability increases considerably just above the cold-point tropopause,  
13 and the tropopause remains near its initial level.

14 A budget analysis reveals that advection contributes to the static stability  
15 tendencies at all times throughout the upper troposphere and lower strato-  
16 sphere. Within the eye, differential advection plays a particularly impor-  
17 tant role in destabilizing the layer near and above the cold-point tropopause.  
18 Outside of the eye, a radial-vertical circulation develops during RI, with  
19 strong outflow below the tropopause and weak inflow above. Vertical wind  
20 shear above and below the upper-tropospheric outflow maximum induces tur-  
21 bulence, which provides forcing for both destabilization and stabilization  
22 in the tropopause layer. Meanwhile, as organized convection reaches the  
23 tropopause, radiative heating tendencies at the top of the cirrus canopy gen-  
24 erally act to destabilize the upper troposphere and stabilize the lower strato-  
25 sphere. Turbulent mixing and radiative heating combine to play an important  
26 role in the development of the strong stable layer immediately above the cold-  
27 point tropopause during RI. The results suggest that turbulence and radiation,  
28 alongside advection, play fundamental roles in the upper-level static stability  
29 evolution of TCs.

## 30 **1. Introduction**

31 Using a high-resolution dropsonde dataset collected during the Tropical Cyclone Intensity ex-  
32 periment (TCI; Doyle et al. 2017), Duran and Molinari (2018) observed dramatic changes in  
33 tropopause structure during the rapid intensification (RI) of Hurricane Patricia (2015). The goal of  
34 the present paper is to analyze the processes that might have produced the upper-tropospheric and  
35 lower-stratospheric fluctuations observed in Patricia using an idealized axisymmetric simulation.

36 After undergoing a remarkably rapid intensification (RI), Hurricane Patricia (2015) set a new  
37 record as the strongest tropical cyclone (TC) ever observed in the Western Hemisphere (Kimber-  
38 lain et al. 2016; Rogers et al. 2017). TCI dropsonde observations collected during this RI period  
39 revealed dramatic changes in the cold-point tropopause height and upper-level static stability (Du-  
40 ran and Molinari 2018). In particular, when Patricia was at tropical storm intensity shortly before  
41 RI commenced, a strong inversion layer existed just above the cold-point tropopause. During the  
42 first half of the RI period, this inversion layer weakened throughout Patricia’s inner core, with the  
43 weakening most pronounced over the developing eye. By the time the storm reached its maximum  
44 intensity of  $95 \text{ m s}^{-1}$ , the inversion layer over the eye had disappeared almost completely, which  
45 was accompanied by a greater than 1-km increase in the tropopause height. Meanwhile over the  
46 eyewall region, the static stability increased and the tropopause remained near its initial level.

47 Despite the importance of tropopause-layer thermodynamics in theoretical models of hurri-  
48 canes (Emanuel and Rotunno 2011; Emanuel 2012), most observational studies of the upper-  
49 tropospheric structure of TCs are decades old. Recently, however, Komaromi and Doyle (2017)  
50 found that stronger TCs tended to have a higher and warmer tropopause over their inner core than  
51 weaker TCs. Their results are consistent with the evolution observed over the inner core of Hur-

52 ricane Patricia, in which the tropopause height increased and the tropopause temperature warmed  
53 throughout RI (Duran and Molinari 2018).

54 Idealized simulations of a TC analyzed by Ohno and Satoh (2015) suggested that the develop-  
55 ment of an upper-level warm core near the 13-km level acted to decrease the static stability near the  
56 tropopause within the eye (compare their Figs. 9,10). Although the mechanisms that might drive  
57 this static stability evolution have not been examined explicitly, Stern and Zhang (2013) described  
58 the development of the TC warm core using a potential temperature ( $\theta$ ) budget analysis. They  
59 found that radial and vertical advection both played important roles in warm core development  
60 throughout RI, and subgrid-scale diffusion became particularly important during the later stage of  
61 RI.

62 Other processes that can modify the static stability in the upper troposphere of TCs include  
63 radiative heating within and near the top of the cirrus canopy and shear-induced turbulent mixing  
64 near the outflow jet. To our knowledge, the only paper that has examined explicitly the static  
65 stability evolution in a modeled TC is Kepert et al. (2016), but their analysis was limited to the  
66 boundary layer. The analysis herein is based upon that of Stern and Zhang (2013), except using a  
67 static stability budget similar to that of Kepert et al. (2016), with a focus on the upper troposphere  
68 and lower stratosphere.

## 69 **2. Model Setup**

70 The numerical simulations were performed using version 19.4 of Cloud Model 1 (CM1) de-  
71 scribed in Bryan and Rotunno (2009). The equations of motion were integrated on a 3000-km-  
72 wide, 30-km-deep axisymmetric grid with 1-km horizontal and 250-m vertical grid spacing. The  
73 computations were performed on an  $f$ -plane at 15°N latitude, over a sea surface with constant  
74 temperature of 30.5°C, which matches that observed near Hurricane Patricia (2015; Kimberlain

et al. 2016). Horizontal turbulence was parameterized using the Smagorinsky scheme described in Bryan and Rotunno (2009, pg. 1773), with a prescribed mixing length that varied linearly from 100 m at a surface pressure of 1015 hPa to 1000 m at a surface pressure of 900 hPa. Vertical turbulence was parameterized using the formulation of Markowski and Bryan (2016, their Eq. 6), using an asymptotic vertical mixing length of 100 m. A Rayleigh damping layer was applied outside of the 2900-km radius and above the 25-km level to prevent spurious gravity wave reflection at the model boundaries. Microphysical processes were parameterized using the Thompson et al. (2004) scheme and radiative heating tendencies were computed every two minutes using the Rapid Radiative Transfer Model for GCMs (RRTMG) longwave and shortwave schemes (Iacono et al. 2008). The initial temperature and humidity field was horizontally homogeneous and determined by averaging all Climate Forecast System Reanalysis (CFSR) grid points within 100 km of Patricia's center of circulation at 18 UTC 21 October 2015. The vortex described in Rotunno and Emanuel (1987, their Eq. 37) was used to initialize the wind field, setting all parameters equal to the values used therein.

Although hurricanes simulated in an axisymmetric framework tend to be more intense than those observed in nature, the intensity evolution of this simulation matches reasonably well with that observed in Hurricane Patricia. After an initial spin-up period of about 20 hours, the modeled storm (Fig. 1, blue lines) began an RI period that lasted approximately 30 hours. After this RI, the storm continued to intensify more slowly until the maximum 10-m wind speed reached  $89 \text{ m s}^{-1}$  and the sea-level pressure reached its minimum of 846 hPa 81 hours into the simulation. Hurricane Patricia (red stars) exhibited a similar intensity evolution prior to its landfall, with an RI period leading to a maximum 10-m wind speed of  $95 \text{ m s}^{-1}$  and a minimum sea-level pressure of 872 hPa.

### 97 3. Budget Computation

98 The static stability can be expressed as the squared Brunt-Väisälä frequency:

$$N_m^2 = \frac{g}{T} \left( \frac{\partial T}{\partial z} + \Gamma_m \right) \left( 1 + \frac{T}{R_d/R_v + q_s} \frac{\partial q_s}{\partial T} \right) - \frac{g}{1 + q_t} \frac{\partial q_t}{\partial z}, \quad (1)$$

99 where  $g$  is gravitational acceleration,  $T$  is temperature,  $R_d$  and  $R_v$  are the gas constants of dry air  
100 and water vapor, respectively,  $q_s$  is the saturation mixing ratio,  $q_t$  is the total condensate mixing  
101 ratio, and  $\Gamma_m$  is the moist-adiabatic lapse rate:

$$\Gamma_m = g(1 + q_t) \left( \frac{1 + L_v q_s / R_d T}{c_{pm} + L_v \partial q_s / \partial T} \right), \quad (2)$$

102 where  $L_v$  is the latent heat of vaporization and  $c_{pm}$  is the specific heat of moist air at constant  
103 pressure. In the tropopause layer,  $q_s$ ,  $\partial q_s / \partial T$ , and  $\partial q_t / \partial z$  approach zero. In this limiting case,  
104 Eq. 1 reduces to:

$$N^2 = \frac{g}{\theta} \frac{\partial \theta}{\partial z}, \quad (3)$$

105 where  $\theta$  is the potential temperature.

106 To compute  $N^2$ , CM1 uses Eq. 1 in saturated environments and Eq. 3 in sub-saturated envi-  
107 ronments. For simplicity, however, only Eq. 3 will be employed for the budget computations  
108 throughout the entire domain<sup>1</sup>.

109 Taking the time derivative of Eq. 3 yields the static stability tendency:

$$\frac{\partial N^2}{\partial t} = \frac{g}{\theta} \frac{\partial}{\partial z} \frac{\partial \theta}{\partial t} - \frac{g}{\theta^2} \frac{\partial \theta}{\partial z} \frac{\partial \theta}{\partial t}, \quad (4)$$

110 where the potential temperature tendency,  $\partial \theta / \partial t$ , can be written, following Bryan (cited 2018):

$$\frac{\partial \theta}{\partial t} = -u \frac{\partial \theta}{\partial r} - w \frac{\partial \theta}{\partial z} + HTURB + VTURB + MP + RAD + DISS \quad (5)$$

111 Each term on the right-hand side of Eq. 5 represents a  $\theta$  budget variable, each of which is output  
112 directly by the model every minute.

---

<sup>1</sup>The validity of this approximation will be substantiated later in this section.

113 The first term on the right-hand side of Eq. 4 is larger than the second term throughout most of  
 114 the tropopause layer (not shown). Consequently, the contribution of each of the terms in Eq. 5 to  
 115 the  $N^2$  tendency can be interpreted in light of a vertical gradient of each term.

116 Taking the vertical gradient of the first two terms on the right-hand side of Eq. 5 yields the time  
 117 tendency of the vertical  $\theta$  gradient due to horizontal and vertical advection<sup>2</sup>:

$$\left( \frac{\partial}{\partial t} \frac{\partial \theta}{\partial z} \right)_{adv} = -u \frac{\partial}{\partial r} \frac{\partial \theta}{\partial z} - w \frac{\partial}{\partial z} \frac{\partial \theta}{\partial z} - \frac{\partial u}{\partial z} \frac{\partial \theta}{\partial r} - \frac{\partial w}{\partial z} \frac{\partial \theta}{\partial z}. \quad (6)$$

118 The first two terms on the right-hand side of Eq. 6 represent advection of static stability by the  
 119 radial and vertical wind, respectively. These terms act to rearrange the static stability field, but  
 120 cannot strengthen or weaken static stability maxima or minima. The third and fourth terms on the  
 121 right-hand side of Eq. 6 represent, respectively, the tilting of isentropes in the presence of vertical  
 122 wind shear, and the stretching or squashing of isentropes by vertical gradients of vertical velocity.  
 123 Since these terms involve velocity gradients, they can act to strengthen or weaken static stability  
 124 maxima or minima through differential advection.

125 Returning to Eq. 5, HTURB and VTURB are the  $\theta$  tendencies from the horizontal and vertical  
 126 turbulence parameterizations, MP is the tendency from the microphysics scheme, RAD is the  
 127 tendency from the radiation scheme, and DISS is the tendency due to turbulent dissipation. This  
 128 equation neglects Rayleigh damping, since the entire analysis domain lies outside of the regions  
 129 where damping is applied. Each term in Eq. 5 is substituted for  $\partial \theta / \partial t$  in Eq. 4, yielding the  
 130 contribution of each budget term to the static stability tendency. These terms are summed, yielding  
 131 an instantaneous "budget change" in  $N^2$  every minute. The budget changes are then averaged over

---

<sup>2</sup>These terms include the tendencies due to implicit diffusion in the fifth-order finite differencing scheme, which are separated from the advection terms in the CM1 budget output

132 24-hour periods and compared to the total model change in  $N^2$  over that same time period, i.e.:

$$\Delta N_{budget}^2 = \frac{1}{\delta t} \sum_{t=t_0}^{t_0+\delta t} \left. \frac{\partial N^2}{\partial t} \right|_t \quad (7)$$

$$\Delta N_{model}^2 = N_{t_0+\delta t}^2 - N_{t_0}^2 \quad (8)$$

$$Residual = \Delta N_{model}^2 - \Delta N_{budget}^2 \quad (9)$$

135 where  $t_0$  is an initial time and  $\delta t$  is 24 hours.

136 Eqs. 7-9 are plotted for three consecutive 24-hour periods in Fig. 2. For this and all subsequent  
 137 radial-vertical cross sections, a 1-2-1 smoother is applied once in the radial direction to eliminate  
 138  $2\Delta r$  noise that appears in some of the raw model output and calculated fields. The left column  
 139 of Fig. 2 depicts the model changes computed using Eq. 8, together with Eq. 1 in saturated envi-  
 140 ronments and Eq. 3 in subsaturated environments. The center column depicts the budget changes  
 141 computed using Eq. 7 together with Eq. 3 throughout the entire domain. Thus, the left column  
 142 includes the effect of moisture in the  $N^2$  computations, whereas the center column neglects mois-  
 143 ture. The right column depicts the residuals, computed using Eq. 9 (i.e. the left column minus  
 144 the center column.) In every 24-hour period, the budget changes are nearly identical to the model  
 145 changes, which is reflected in the near-zero residuals in the right column. This indicates that the  
 146 budget accurately represents the model variability, which implies that the neglect of moisture in  
 147 the budget computation introduces negligible error within the analysis domain<sup>3</sup>.

148 In the tropopause layer, some of the budget terms are small enough to be ignored. To determine  
 149 which of the budget terms are most important, a time series of the contribution of each of the  
 150 budget terms in Eq. 5 to the tropopause-layer static stability tendency is plotted in Fig. 3. For this  
 151 figure, each of the budget terms is computed using the method described in Section 3, except with

---

<sup>3</sup>This is not the case in the lower- and mid-troposphere, where the residual actually exceeds the budget tendencies in many places, likely due to the neglect of moisture; thus we limit this analysis to the upper troposphere and lower stratosphere.



152 1-hour averaging intervals instead of 24-hour intervals. The absolute values of these tendencies  
153 are then averaged over the radius-height domain of the plots shown in Fig. 2 and plotted as a time  
154 series<sup>4</sup>. Advection (Fig. 3, red line) plays an important role in the mean tropopause-layer static  
155 stability tendency at all times, and vertical turbulence (Fig. 3, blue line) and radiation (Fig. 3, dark  
156 green line) also contribute significantly. The remaining three processes - horizontal turbulence,  
157 microphysics, and dissipative heating - are negligible everywhere outside of the eyewall, and do  
158 not play important roles in the mesoscale tropopause variability.

159 The preceding analysis indicates that, at all times, three budget terms dominate the tropopause-  
160 layer static stability tendency: advection, vertical turbulence, and radiation. Variations in the  
161 magnitude and spatial structure of these terms drive the static stability changes depicted in Fig. 2;  
162 subsequent sections will focus on these variations and what causes them.

## 163 4. Results

### 164 a. Static stability evolution

165 The average  $N^2$  over the first day of the simulation (Fig. 4a) indicates the presence of a weak  
166  $N^2$  maximum just above the cold-point tropopause. Over the subsequent 24 hours, during the  
167 RI period, the  $N^2$  within and above this layer decreased within the 25-km radius (Fig. 4b). This  
168 decreasing  $N^2$  corresponded to an increase in the tropopause height within the developing eye,  
169 maximized at the storm center. Outside of the eye, meanwhile, the tropopause height decreased  
170 over the eyewall region (25-60-km radius) and increased only slightly outside of the 60-km ra-  
171 dius. In this outer region, the  $N^2$  maximum just above the tropopause strengthened during RI.

---

<sup>4</sup>It will be seen in subsequent figures that each of the terms contributes both positively and negatively to the  $N^2$  tendency within the analysis domain. Thus, taking an average over the domain tends to wash out the positive and negative contributions. To circumvent this problem, the absolute value of each of the terms is averaged.

172 These trends continued as the storm's intensity leveled off in the 48-72-hour period (Fig. 4c). The  
 173 tropopause height increased to nearly 21 km at the storm center and sloped sharply downward to  
 174 16.3 km on the inner edge of the eyewall, near the 30 km radius. Static stability outside of the eye,  
 175 meanwhile, continued to increase just above the cold-point tropopause. This  $N^2$  evolution closely  
 176 follows that observed in Hurricane Patricia (2015; Duran and Molinari 2018, see their Fig. 4). The  
 177 mechanisms that led to these  $N^2$  changes will be investigated in the subsequent sections.

## 178 *b. Static stability budget analysis*

### 179 *(i) 0-24 hours*

180 The initial spin-up period was characterized by a steady increase of the maximum wind speed  
 181 from 11 m s<sup>-1</sup> to 22 m s<sup>-1</sup> (Fig. 1a, blue line), an intensification rate that closely matched that of  
 182 TC Patricia (Fig. 1a, red stars). The weakening of the lower-stratospheric  $N^2$  maximum during  
 183 this period is reflected in the total  $N^2$  budget change over this time (Fig. 5a). The layer just above  
 184 the cold-point tropopause was characterized by decreasing  $N^2$  (purple shading), maximizing at the  
 185 storm center. At and immediately below the tropopause, meanwhile, saw increasing  $N^2$  during this  
 186 time period. Although these tendencies extended out to the 200-km radius, they were particularly  
 187 pronounced at innermost radii. A comparison of the contributions of advection (Fig. 5b), vertical  
 188 turbulence (Fig. 5c), and radiation (Fig. 5d) reveals that advection was the primary driver of the  
 189  $N^2$  tendency during this period, acting to stabilize near and just below the tropopause and destabi-  
 190 lize above. Although vertical turbulence acted in opposition to advection (i.e. it acted to stabilize  
 191 regions that advection acted to destabilize), the magnitude of the advective tendencies was larger,  
 192 particularly at the innermost radii. The sum of advection and vertical turbulence (Fig. 5e) almost  
 193 exactly replicated the static stability tendencies above the tropopause. Radiative tendencies, mean-  
 194 while, (Fig. 5d) acted to destabilize the layer below about 16 km and stabilize the layer between

16 and 17 km. The sum of advection, vertical turbulence, and radiation (Fig. 5f) reproduced the total change in  $N^2$  almost exactly.

(ii) 24-48 hours

During the RI period, the maximum wind speed increased from  $22 \text{ m s}^{-1}$  to  $80 \text{ m s}^{-1}$ . Over this time,  $N^2$  within the eye generally decreased above 16 km and increased below (Fig. 6a), with the destabilization above 16 km maximizing near the level of the mean cold-point tropopause. These tendencies at the innermost radii were driven almost entirely by advection (Fig. 6b). Vertical turbulence (Fig. 6c) and radiation (Fig. 6d) contributed negligibly to the static stability tendencies in this region.

Outside of the eye, the  $N^2$  evolution exhibited alternating layers of positive and negative tendencies. Near and above 18 km existed an upward-sloping region of decreasing  $N^2$  that extended out to the 180-km radius. In this region, neither vertical turbulence nor radiation exhibited negative  $N^2$  tendencies; advection was the only forcing for this destabilization. Immediately below this layer, just above the cold-point tropopause, was a region of increasing  $N^2$  that sloped upward from 17 km near the 30-km radius to just below 18 km outside of the 100-km radius. Advection and vertical turbulence both contributed to this positive  $N^2$  tendency, with advection playing an important role below about 17.5 km and turbulence playing an important role above. The sum of advection and turbulence (Fig. 6e) reveals two discontinuous regions of increasing  $N^2$  in the 17-18-km layer rather than one contiguous region. The addition of radiation to these two terms, however, (Fig. 6f) provides the link between these two regions, indicating that radiation also plays a role in strengthening the stable layer just above the tropopause. In the 16-17-km layer, just below the cold-point tropopause, a horizontally-extensive layer of destabilization also was forced by a combination of advection, vertical turbulence, and radiation. The sum of advection and vertical turbulence ac-

counts for only a portion of the decreasing  $N^2$  in this layer, and actually indicates forcing for stabilization near the 50-km radius and outside of the 130-km radius. Radiative tendencies overcome this forcing for stabilization in both of these regions to produce the radially-extensive region of destabilization observed just below the tropopause.

The sum of advection, vertical turbulence, and radiation (Fig. 6f) once again closely follows the observed  $N^2$  variability, except in the eyewall region, where the neglect of latent heating and horizontal turbulence introduces some differences.

### (iii) 48-72 hours

After the storm's maximum wind speed leveled off near  $80 \text{ m s}^{-1}$ , the magnitude of the static stability tendencies within the eye decreased to near zero (Fig. 7a).

Outside of the eye, however,  $N^2$  continued to decrease in the layer immediately surrounding the tropopause. The sum of advection and vertical turbulence (Fig. 7e) indicates that the increase of  $N^2$  observed in the 17-18-km layer and inside of the 80-km radius cannot be attributed to these processes, since the sum of these two terms provided forcing for destabilization. Instead, radiation (Fig. 7d) provided the forcing for stabilization in this region. Outside of the 80-km radius, both advection (Fig. 7b) and vertical turbulence (Fig. 7c) provided forcing for stabilization near and just above the 18-km level. The sum of the two terms (Fig. 7e) indicates increasing  $N^2$  near the 18-km level everywhere outside of the 80-km radius, but this stabilization is slightly weaker in the 90-120-km radial band than the observed value. The addition of radiation (Fig. 7f) provided the extra forcing for stabilization required to account for the observed increase in  $N^2$ . Outside of the 120-km radius, the region of radiative forcing for stabilization sloped downward, and the increase in  $N^2$  observed near 18 km can be explained entirely by a combination of advection and vertical turbulence. The layer of decreasing  $N^2$  observed near the tropopause was forced primarily

241 by vertical turbulence and radiation. Within most of this region, advection provided strong forcing  
242 for stabilization, but this forcing was outweighed by the negative  $N^2$  tendencies induced by a  
243 combination of vertical turbulence and radiation.

## 244 5. Discussion

### 245 *a. The role of advection*

246 Advection played an important role in the tropopause-layer  $N^2$  evolution at all stages of intensi-  
247 fication, but for brevity, this section will focus only on the RI (24-48-hour) period. To investigate  
248 the advective processes more closely, the individual contributions of horizontal and vertical advec-  
249 tion during the RI period are shown in Fig. 8, along with the corresponding time-mean radial and  
250 vertical velocities and  $\theta$ . The  $N^2$  tendencies due to the two advective components (Fig. 8a,b) ex-  
251 hibited strong cancellation, consistent with flow that was nearly isentropic. There were, however,  
252 many regions in which flow crossed  $\theta$  surfaces; this flow accounted for all non-zero  $N^2$  tendencies  
253 due to advection previously seen in Fig. 6b.

254 During the RI period, strong radial and vertical circulations developed near the tropopause  
255 (Fig. 8c,d), which forced high-magnitude  $N^2$  tendencies due to advection (Fig. 8a,b). A layer  
256 of strong outflow formed at and below the tropopause during this period, with the outflow maxi-  
257 mum (dashed cyan line) curving from the 14-km level at the 50-km radius to just below the 16-km  
258 level outside of the 80-km radius (Fig. 8c). Notably, the  $N^2$  tendency due to horizontal advec-  
259 tion (Fig. 8a) tended to switch signs at this line, with stabilization below the outflow maximum  
260 and destabilization above. This is consistent with the outflow layer carrying air with increasingly  
261 large  $\theta$  from the eyewall to large radii as the storm intensified. This increase in  $\theta$  maximized near  
262 the outflow maximum, which acted to decrease  $\partial\theta/\partial z$  above the outflow maximum and increase

263 it below. This mechanism is the same as that discussed in Trier and Sharman (2009), in which  
264 vertical wind shear in the outflow layer of a mesoscale convective system acted to modify the  
265 upper-tropospheric static stability through differential advection of isentropes.

266 Meanwhile in the lower stratosphere, a thin layer of  $2\text{--}4\text{ m s}^{-1}$  inflow developed a few hundred  
267 meters above the tropopause, similar to that which was observed in Hurricane Patricia (2015;  
268 Duran and Molinari 2018) and in previous modeling studies (e.g. Ohno and Satoh 2015; Kieu et al.  
269 2016). Since the isentropes in this layer sloped slightly upward with radius (i.e.  $\partial\theta/\partial r < 0$ ), this  
270 inflow acted to import lower  $\theta$  air from outer radii to inner radii. Since the negative  $\theta$  tendencies  
271 maximized at the level of maximum inflow, the layer below the inflow maximum destabilized and  
272 the layer above stabilized (Fig. 8a).

273 Curiously, horizontal advection contributed to the  $N^2$  tendency everywhere within the eye,  
274 even though the mean radial velocity there was near zero. Close examination of the model out-  
275 put revealed that these tendencies were forced by advective processes associated with inward-  
276 propagating waves. Although the radial velocity perturbations induced by these waves averaged  
277 out to zero, the advective tendencies forced by the radial velocity perturbations did not. Addition-  
278 ally, when these waves reached  $r=0$ , a dipole of vertical velocity resulted, with ascent above and  
279 descent below. For reasons that remain unclear, the regions of ascent were more persistent than the  
280 regions of descent, which resulted in the mean ascent observed near  $r=0$  above 17 km in Fig. 8b.

281 Vertical advection also played an important role in the tropopause-layer static stability evolution.  
282 Within the eye, subsidence dominated below 17 km, while mean ascent existed near the storm  
283 center above 17 km. Although the magnitude of the subsidence was larger at lower altitudes,  
284  $\partial\theta/\partial z$  was smaller there. Because  $\partial\theta/\partial z$  was smaller, the subsidence at lower levels could not  
285 accomplish as much warming as the subsidence at higher levels in the eye, consistent with the

286 results of Stern and Zhang (2013). As a result, vertical advection within the eye acted to stabilize  
287 the layer below 16 km during RI.

288 Outside of the 27-km radius, ascent dominated the troposphere, while a 1.5-km-deep layer of  
289 descent existed immediately above the tropopause. These regions of ascent and descent converged  
290 just above the tropopause; this convergence acted to compact the isentropes in this layer and in-  
291 crease the static stability. Above the lower-stratospheric subsidence maximum, meanwhile, verti-  
292 cal advection acted to decrease  $N^2$ . Below the tropopause, differential vertical advection increased  
293  $N^2$  within the eyewall region and also at larger radii above the vertical velocity maximum at larger  
294 radii. Outside of the eyewall and below the vertical velocity maximum, meanwhile, differential  
295 vertical advection acted to decrease  $N^2$ .

296 Comparing the  $N^2$  tendencies forced by horizontal (Fig. 8a) and vertical (Fig. 8b) advection  
297 to the total advective tendency seen in Fig. 6b reveals that horizontal advective tendencies domi-  
298 nated the troposphere, while vertical advective tendencies dominated the layer near and above the  
299 tropopause. Thus, tilting of isentropes in the vicinity of the upper-tropospheric outflow maximum  
300 appears to be the most important process governing the  $N^2$  tendency in the troposphere, whereas  
301 convergence of vertical velocity appears to be the most important process near the tropopause.

## 302 *b. The role of radiation*

303 During the initial spin-up period (0-24 hours; Fig. 9a), convection was not deep enough to  
304 deposit large quantities of ice near the tropopause and create a persistent cirrus canopy. Due to the  
305 lack of ice particles, the radiative heating tendencies during this period (Fig. 9b) were relatively  
306 small and confined to the region above a few particularly strong, although transient, convective  
307 towers. During RI (24-48 hours), the eyewall updraft strengthened and a radially-extensive cirrus  
308 canopy developed near the tropopause (Fig. 9c). The enhanced vertical gradient of ice mixing ratio

309 at the top of the cirrus canopy induced strong diurnal-mean radiative cooling near the tropopause  
310 (Fig. 9d). This cooling exceeded  $0.6 \text{ K h}^{-1}$  in some places and sloped downward from the lower  
311 stratosphere into the upper troposphere, following the top of the cirrus canopy. A small radiative  
312 warming maximum also appeared outside of the 140-km radius below this region of cooling. These  
313 results broadly agree with those of Bu et al. (2014; see their Fig. 11a), whose CM1 simulations  
314 produced a  $0.3 \text{ K h}^{-1}$  diurnally-averaged radiative cooling at the top of the cirrus canopy and  
315 radiative warming within the cloud that maximized near the 200-km radius. This broad region  
316 of radiative cooling acted to destabilize the layer below the cooling maximum and stabilize the  
317 layer above, which can be seen in Fig. 6d. The small area of net radiative heating outside of the  
318 140-km radius enhanced the destabilization above 16 km in this region and produced a thin layer  
319 of stabilization in the 15-16-km layer.

320 After the TC's RI period completed (48-72 hours), strong radiative cooling remained near the  
321 tropopause at inner radii (Fig. 9f), sloping downward with the top of the cirrus canopy to below  
322 the tropopause at outer radii. Cooling rates exceeded  $1 \text{ K h}^{-1}$  just above the tropopause between  
323 the 30- and 70-km radii. This value is more than three times the maximum cooling rate of  $0.3 \text{ K h}^{-1}$   
324 observed by Bu et al. (2014), a discrepancy that is a consequence of their larger vertical grid  
325 spacing compared to that used here, along with a contribution from differing radiation schemes. To  
326 compare our results to those of Bu et al. (2014), we ran a simulation identical to that described in  
327 Section 2, except using the NASA-Goddard radiation scheme and 625-m vertical grid spacing, to  
328 match those of Bu et al. (2014). This simulation produced a maximum 24-hour-average radiative  
329 cooling rate of  $0.3 \text{ K h}^{-1}$ , which agrees with that shown in Bu et al. (2014). Another simulation  
330 using 625-m vertical grid spacing and RRTMG radiation produced 24-hour-average cooling rates  
331 of up to  $0.6 \text{ K h}^{-1}$ , which is consistent with the WRF simulations of Bu et al. (2014). This suggests  
332 that vertical grid spacing smaller than 625 m is necessary to resolve properly the radiative cooling



333 at the top of the cirrus canopy, and that the results can be quite sensitive to the radiation scheme  
334 used.

335 Meanwhile below the tropopause, time-mean radiative warming spread from 30- to 160-km  
336 radius within the cirrus canopy. The existence of radiative cooling overlying radiative warming in  
337 this region led to radiatively-forced destabilization at and below the tropopause, as was observed  
338 in Fig. 7d. Beneath the warming layer existed a region of forcing for stabilization, while a much  
339 stronger region of forcing for stabilization existed in the lower stratosphere, above the cooling  
340 maximum.

341 The results herein suggest that radiative heating tendencies played an important role in destabi-  
342 lizing the upper troposphere and stabilizing the lower stratosphere after the cirrus canopy devel-  
343 oped.

### 344 *c. The role of turbulent mixing*

345 Although vertical turbulence always acts to eliminate vertical gradients of  $\theta$ , this adjustment  
346 toward a neutral state only occurs where the mixing takes place. If turbulence occurs in a stably-  
347 stratified layer, it will act to decrease  $\theta$  at the top of the layer and increase it below. Just above and  
348 just below the mixed layer, however, the  $\theta$  profile remains undisturbed. Consequently, although  
349 turbulent mixing acts to decrease  $\partial\theta/\partial z$  in the layer in which it is occurring, it actually increases  
350  $\partial\theta/\partial z$  just below and just above the layer. These vertical gradients of turbulent mixing are quite  
351 important, particularly on the flanks of the upper-tropospheric outflow jet.

352 Two distinct maxima of vertical eddy diffusivity developed in the tropopause layer as the storm  
353 intensified (Fig. 10). Comparison of these turbulent regions to the  $N^2$  tendencies in Figs. 6c and  
354 7c reveals that the layers in which vertical eddy diffusivity maximized corresponded to layers of  
355 destabilization due to vertical turbulence. Just outside of these layers, however, vertical turbulence

acted to increase  $N^2$ . The large vertical gradient of vertical eddy diffusivity near the tropopause played an important role in developing the lower-stratospheric stable layer during RI. This supports the hypothesized role of turbulence in setting the outflow-layer  $\theta$  stratification in Rotunno and Emanuel (1987).

## 6. Conclusions

The simulated  $N^2$  evolution shown herein closely matched that observed during the RI of Hurricane Patricia (2015). Three processes dominated the  $N^2$  variability in the upper troposphere and lower stratosphere: advection, radiation, and vertical turbulence. Radiation and vertical turbulence played particularly important roles in developing the strong  $N^2$  maximum just above the cold-point tropopause during RI. Since these two processes are parameterized, and radiation closely depends on yet another parameterized process (microphysics), the tropopause-layer  $N^2$  variability could be quite sensitive to the assumptions inherent to the parameterizations used. A better understanding of the microphysical characteristics of the TC cirrus canopy, its interaction with radiation, and outflow-layer turbulence is critical to understanding the tropopause-layer  $N^2$  evolution.

In this paper, all of the variables were averaged over a full diurnal cycle to eliminate the effects of diurnal variability and isolate the overall storm evolution. Diurnal variations in static stability near the tropopause are potentially of interest with respect to the tropical cyclone diurnal cycle, however, and will be the subject of future work.

*Acknowledgments.* We are indebted to George Bryan for his continued development and support of Cloud Model 1. We also thank Jeffrey Kepert, Robert Fovell, and Erika Navarro for helpful conversations related to this work. This research was supported by NSF Grant #1636799.

## APPENDIX

## Sensitivity experiments

The simulations exhibited some sensitivity to the initial thermodynamic profile and the prescribed vertical mixing length. Although the details of the intensification and the tropopause-layer  $N^2$  evolution varied when these quantities were changed, the conclusions of the paper remain unchanged.

### *a. Sensitivity to the initial thermodynamic profile*

A number of sensitivity experiments were conducted using a variety of initial soundings. Changing the initial temperature and humidity profiles affected the timing of the onset of organized deep convection and the rapidity of intensification. In all simulations, however, convection eventually penetrated to the tropopause, at which time vertical turbulence and radiation combined with advection to adjust the  $N^2$  profile toward that which was observed in the control run. By the end of the RI period in every simulation, all three processes were actively modifying the  $N^2$  profile near the tropopause.

As an example, 24-hour averages of  $N^2$  are plotted in Fig. A1 for a simulation that was identical to that used in this paper, except the initial sounding was determined by averaging every CFSR grid point within 1000 km of TC Patricia's storm center at 18 UTC 21 October 2015 instead of averaging only within the 100-km radius. Although the lower-stratospheric stable layer developed more slowly and was weaker than that shown in Fig. 4, the overall evolution was quite similar and the same budget terms dominated the  $N^2$  evolution.

### *b. Sensitivity to the vertical mixing length*

The rate of turbulent mixing in the Smagorinsky scheme used herein is highly dependent on a prescribed length scale. The vertical mixing length used in this paper (100 m) was based on the

sensitivity experiments of Bryan (2012). Prescribing a smaller mixing length produces smaller  $\theta$  tendencies due to turbulence, but even with a mixing length on the low end of those tested by Bryan (2012), turbulence still played an important role in the tropopause-layer  $N^2$  evolution. Fig. A2 shows the 24-hour-averaged contributions of turbulent mixing to the  $N^2$  evolution from a simulation identical to that used in this paper, except with a vertical mixing length of 50 m. At all times, vertical turbulence still played an important role in the tropopause-layer  $N^2$  evolution, particularly during the latter stages of RI (48-72 hours).

## References

- Bryan, G. H., 2012: Effects of surface exchange coefficients and turbulence length scales on the intensity and structure of numerically simulated hurricanes. *Mon. Wea. Rev.*, **140**, 1125–1143.
- Bryan, G. H., cited 2018: The governing equations for CM1. [Available online at [http://www2.mmm.ucar.edu/people/bryan/cm1/cm1\\_equations.pdf](http://www2.mmm.ucar.edu/people/bryan/cm1/cm1_equations.pdf)].
- Bryan, G. H., and R. Rotunno, 2009: The maximum intensity of tropical cyclones in axisymmetric numerical model simulations. *Mon. Wea. Rev.*, **137**, 1770–1789.
- Bu, Y. P., R. G. Fovell, and K. L. Corbosiero, 2014: Influence of cloud-radiative forcing on tropical cyclone structure. *J. Atmos. Sci.*, **71**, 1644–1622.
- Doyle, J. D., and Coauthors, 2017: A view of tropical cyclones from above: The Tropical Cyclone Intensity (TCI) Experiment. *Bull. Amer. Meteor. Soc.*, **98**, 2113–2134.
- Duran, P., and J. Molinari, 2018: Dramatic inner-core tropopause variability during the rapid intensification of Hurricane Patricia (2015). *Mon. Wea. Rev.*, **146**, 119–134.
- Emanuel, K., 2012: Self-stratification of tropical cyclone outflow. Part II: Implications for storm intensification. *J. Atmos. Sci.*, **69**, 988–996.

422 Emanuel, K., and R. Rotunno, 2011: Self-stratification of tropical cyclone outflow. Part I: Impli-  
 423 cations for storm structure. *J. Atmos. Sci.*, **68**, 2236–2249.

424 Iacono, M. J., J. S. Delamere, E. J. Mlawer, M. W. Shephard, S. A. Clough, and W. D. Collins,  
 425 2008: Radiative forcing by long-lived greenhouse gases: Calculations with the AER radiative  
 426 transfer models. *J. Geophys. Res.*, **113** (D13103).

427 Kepert, J. D., J. Schwendike, and H. Ramsay, 2016: Why is the tropical cyclone boundary layer  
 428 not ”well mixed”? *J. Atmos. Sci.*, **73**, 957–973.

429 Kieu, C., V. Tallapragada, D.-L. Zhang, and Z. Moon, 2016: On the development of double warm-  
 430 core structures in intense tropical cyclones. *J. Atmos. Sci.*, **73**, 4487–4506.

431 Kimberlain, T. B., E. S. Blake, and J. P. Cangialosi, 2016: Tropical cyclone report: Hurricane  
 432 Patricia. National Hurricane Center. [Available online at [www.nhc.noaa.gov](http://www.nhc.noaa.gov)].

433 Komaromi, W. A., and J. D. Doyle, 2017: Tropical cyclone outflow and warm core structure as  
 434 revealed by HS3 dropsonde data. *Mon. Wea. Rev.*, **145**, 1339–1359.

435 Markowski, P. M., and G. H. Bryan, 2016: LES of laminar flow in the PBL: A potential problem  
 436 for convective storm simulations. *Mon. Wea. Rev.*, **144**, 1841–1850.

437 Ohno, T., and M. Satoh, 2015: On the warm core of a tropical cyclone formed near the tropopause.  
 438 *J. Atmos. Sci.*, **72**, 551–571.

439 Rogers, R. F., S. Aberson, M. M. Bell, D. J. Cecil, J. D. Doyle, J. Morgerman, L. K. Shay, and  
 440 C. Velden, 2017: Re-writing the tropical record books: The extraordinary intensification of  
 441 Hurricane Patricia (2015). *Bull. Amer. Meteor. Soc.*, **98**, 2091–2112.

442 Rotunno, R., and K. A. Emanuel, 1987: An air-sea interaction theory for tropical cyclones. Part II:  
443 Evolutionary study using a nonhydrostatic axisymmetric numerical model. *J. Atmos. Sci.*, **44**,  
444 542–561.

445 Stern, D. P., and F. Zhang, 2013: How does the eye warm? Part I: A potential temperature budget  
446 analysis of an idealized tropical cyclone. *J. Atmos. Sci.*, **70**, 73–89.

447 Thompson, G., R. M. Rasmussen, and K. Manning, 2004: Explicit forecasts of winter precipitation  
448 using an improved bulk microphysics scheme. Part I: Description and sensitivity analysis. *Mon.*  
449 *Wea. Rev.*, **132**, 519–542.

450 Trier, S. B., and R. D. Sharman, 2009: Convection-permitting simulations of the environment sup-  
451 porting widespread turbulence within the upper-level outflow of a mesoscale convective system.  
452 *Mon. Wea. Rev.*, **137**, 1972–1990.

## LIST OF FIGURES

- Fig. 1.** The maximum 10-m wind speed (top panel;  $\text{m s}^{-1}$ ) and minimum sea-level pressure (bottom panel; hPa) in the simulated storm (blue lines; plotted every minute) and from Hurricane Patricia's best track (red stars; plotted every six hours beginning at the time Patricia attained tropical storm intensity). The rapid weakening during the later stage of Patricia's lifetime was induced by landfall. . . . . 25
- Fig. 2.** Left panels: Twenty-four-hour changes in squared Brunt-Väisälä frequency ( $N^2$ ;  $10^{-4} \text{ s}^{-2}$ ) computed using Eq. 8 over (top row) 0-24 hours, (middle row) 24-48 hours, (bottom row) 48-72 hours. Middle Panels: The  $N^2$  change over the same time periods computed using Eqs. 4-7, Right Panels: The budget residual over the same time periods, computed by subtracting the budget change (middle column) from the model change (left column). Orange lines represent the cold-point tropopause height averaged over the same time periods. . . . . 26
- Fig. 3.** Time series of the contribution of each of the budget terms to the time tendency of the squared Brunt-Väisälä frequency ( $N^2$ ;  $10^{-4} \text{ s}^{-2}$ ). For each budget term, the absolute value of the  $N^2$  tendency is averaged temporally over 1-hour periods (using output every minute), and spatially in a region extending from 0 to 200 km radius and 14 to 21 km altitude. . . . . 27
- Fig. 4.** Twenty-four-hour averages of squared Brunt-Väisälä frequency ( $N^2$ ;  $10^{-4} \text{ s}^{-2}$ ) over (a) 0-24 hours, (b) 24-48 hours, (c) 48-72 hours. Orange lines represent the cold-point tropopause height averaged over the same time periods. . . . . 28
- Fig. 5.** (a) Total change in  $N^2$  over the 0-24-hour period ( $10^{-4} \text{ s}^{-2} (24 \text{ h})^{-1}$ ) and the contributions to that change from (b) the sum of horizontal and vertical advection, (c) vertical turbulence, (d) longwave and shortwave radiation, (e) the sum of horizontal advection, vertical advection, and vertical turbulence, and (f) the sum of horizontal advection, vertical advection, vertical turbulence, and longwave and shortwave radiation. Orange lines represent the cold-point tropopause height averaged over the 0-24-hour period. . . . . 30
- Fig. 6.** As in Fig. 5, but for the 24-48-hour period. . . . . 31
- Fig. 7.** As in Fig. 5, but for the 48-72-hour period. . . . . 32
- Fig. 8.** The contributions to the change in  $N^2$  over the 24-48-hour period ( $10^{-4} \text{ s}^{-2} (24 \text{ h})^{-1}$ ) by (a) horizontal advection and (b) vertical advection. (c) The radial velocity ( $\text{m s}^{-1}$ ; filled contours), potential temperature (K; thick black contours), cold-point tropopause height (orange line), and level of maximum outflow (dashed cyan line) averaged over the 24-48-hour period. (d) The vertical velocity ( $\text{cm s}^{-1}$ ; filled contours), potential temperature (K; thick black contours), and cold-point tropopause height (orange line) averaged over the 24-48-hour period. 33
- Fig. 9.** Ice mixing ratio ( $\text{g kg}^{-1}$ ) and cold-point tropopause height (orange lines) averaged over (a) 0-24 hours, (c) 24-48 hours, and (e) 48-72 hours. Radiative heating rate ( $\text{K h}^{-1}$ ) and cold-point tropopause height (orange lines) averaged over (b) 0-24 hours, (d) 24-48 hours, and (f) 48-72 hours. . . . . 35
- Fig. 10.** Vertical eddy diffusivity ( $\text{m}^2 \text{ s}^{-2}$ ; filled contours), cold-point tropopause height (cyan lines), and radial velocity ( $\text{m s}^{-1}$ ; thick black lines) averaged over (a) 0-24 hours, (b) 24-48 hours, and (c) 48-72 hours. . . . . 36

494 **Fig. A1.** Twenty-four-hour averages of squared Brunt-Väisälä frequency ( $N^2$ ;  $10^{-4} \text{ s}^{-2}$ ) over (a) 0-24  
495 hours, (b) 24-48 hours, (c) 48-72 hours, and (d) 72-96 hours for the simulation described  
496 in Appendix Aa. Orange lines represent the cold-point tropopause height averaged over the  
497 same time periods. . . . . 37

498 **Fig. A2.** The contribution of vertical turbulence to the  $N^2$  variability ( $10^{-4} \text{ s}^{-2} (24 \text{ h})^{-1}$ ) averaged  
499 over (a) 0-24 hours, (b) 24-48 hours, (c) 48-72 hours, and (d) 72-96 hours for the simulation  
500 described in Appendix Ab. Orange lines represent the cold-point tropopause height averaged  
501 over the same time periods. . . . . 38



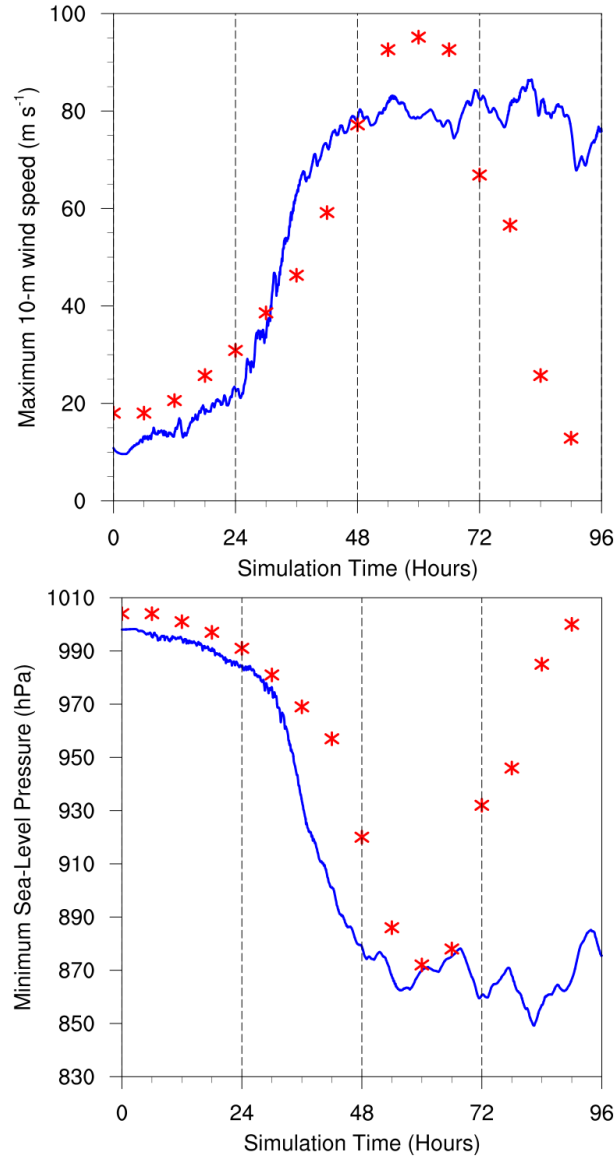


FIG. 1. The maximum 10-m wind speed (top panel;  $\text{m s}^{-1}$ ) and minimum sea-level pressure (bottom panel; hPa) in the simulated storm (blue lines; plotted every minute) and from Hurricane Patricia's best track (red stars; plotted every six hours beginning at the time Patricia attained tropical storm intensity). The rapid weakening during the later stage of Patricia's lifetime was induced by landfall.

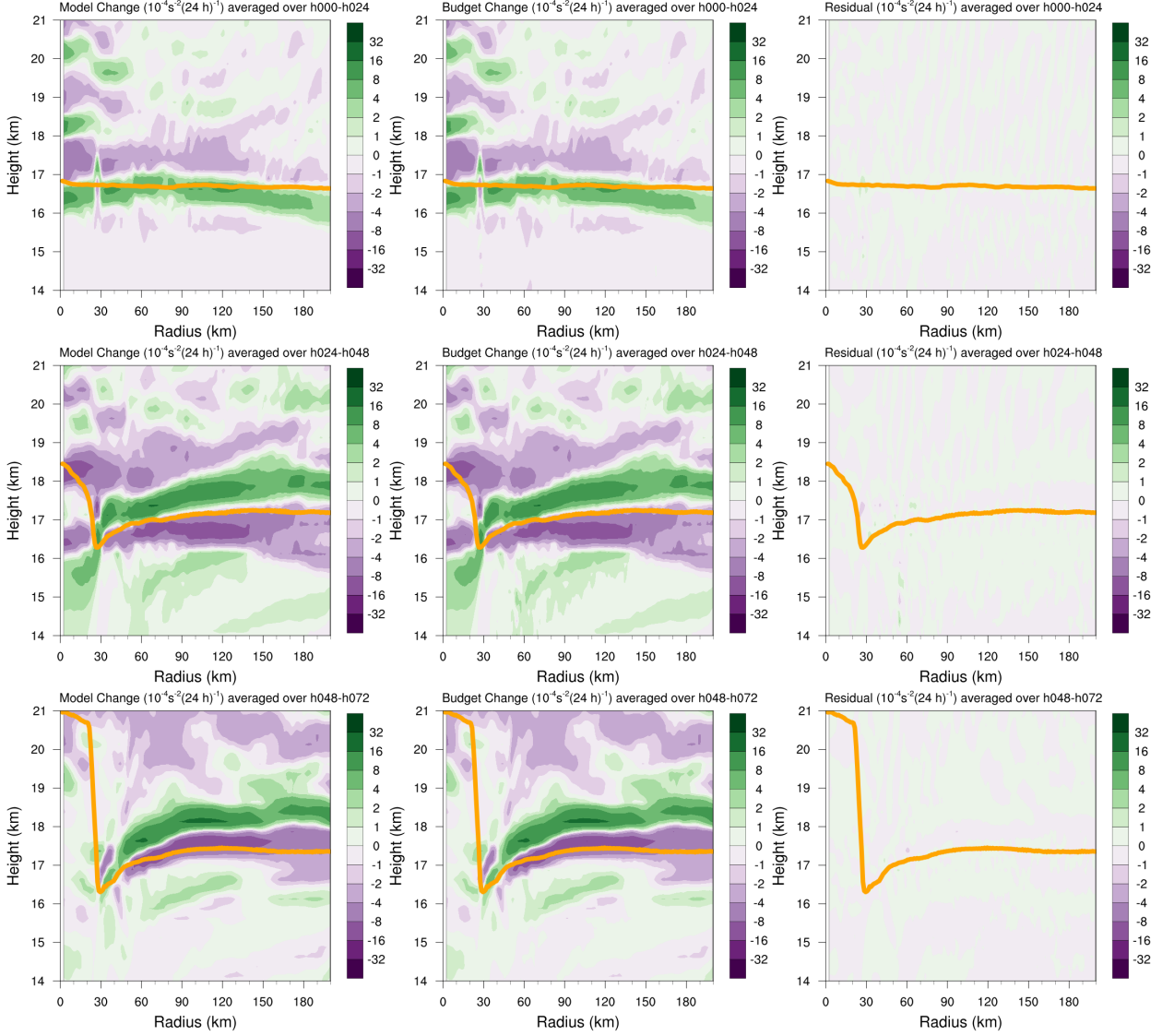


FIG. 2. Left panels: Twenty-four-hour changes in squared Brunt-Väisälä frequency ( $N^2$ ;  $10^{-4} \text{ s}^{-2}$ ) computed using Eq. 8 over (top row) 0-24 hours, (middle row) 24-48 hours, (bottom row) 48-72 hours. Middle Panels: The  $N^2$  change over the same time periods computed using Eqs. 4-7, Right Panels: The budget residual over the same time periods, computed by subtracting the budget change (middle column) from the model change (left column). Orange lines represent the cold-point tropopause height averaged over the same time periods.

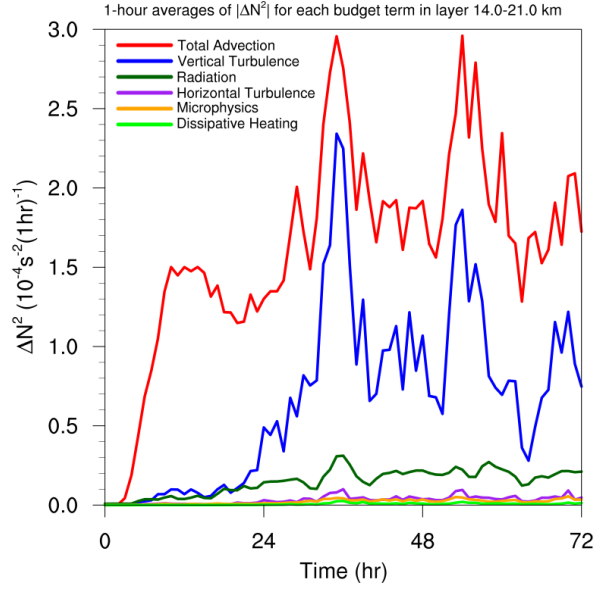


FIG. 3. Time series of the contribution of each of the budget terms to the time tendency of the squared Brunt-Väisälä frequency ( $N^2$ ;  $10^{-4} \text{ s}^{-2}$ ). For each budget term, the absolute value of the  $N^2$  tendency is averaged temporally over 1-hour periods (using output every minute), and spatially in a region extending from 0 to 200 km radius and 14 to 21 km altitude.

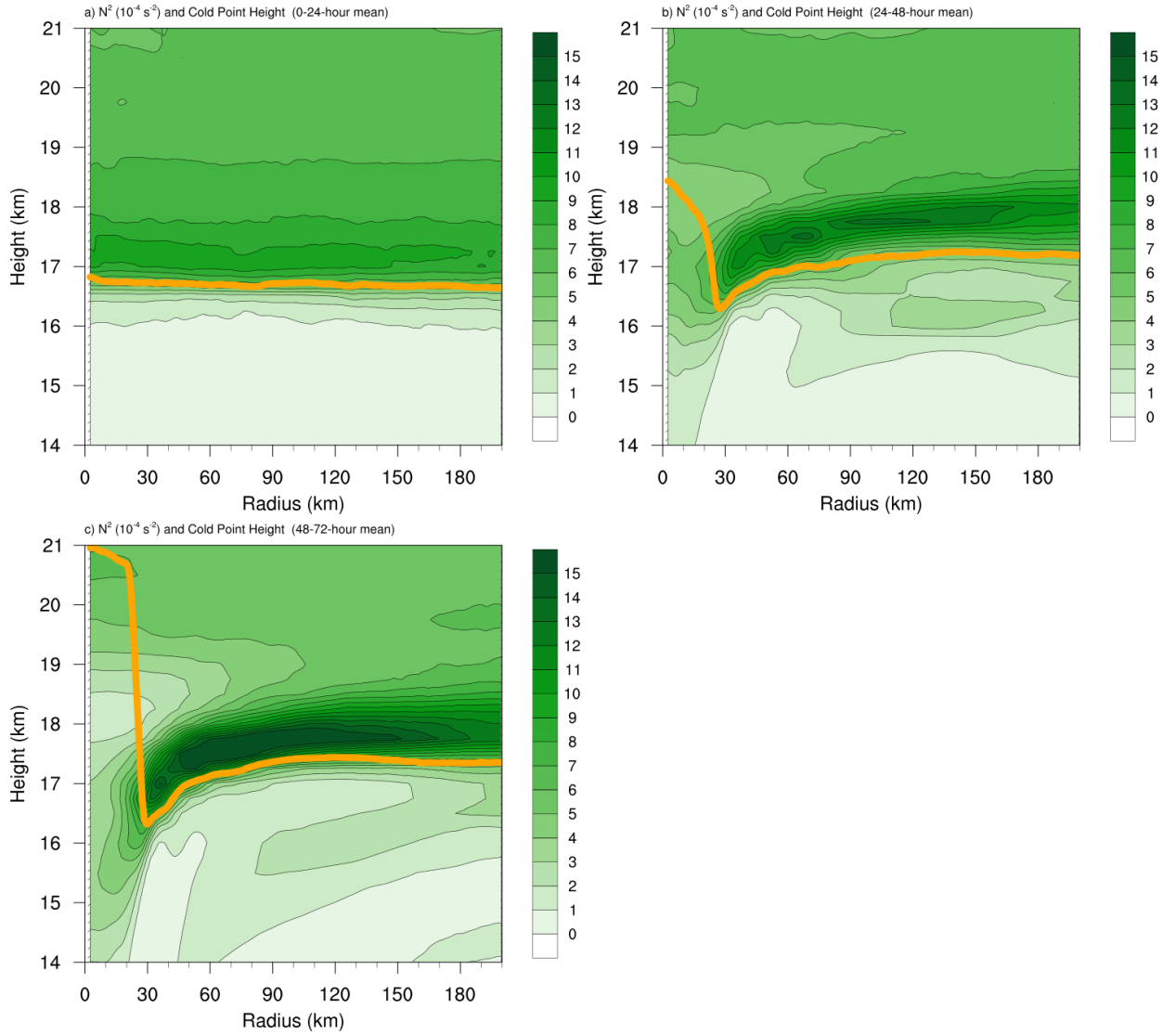
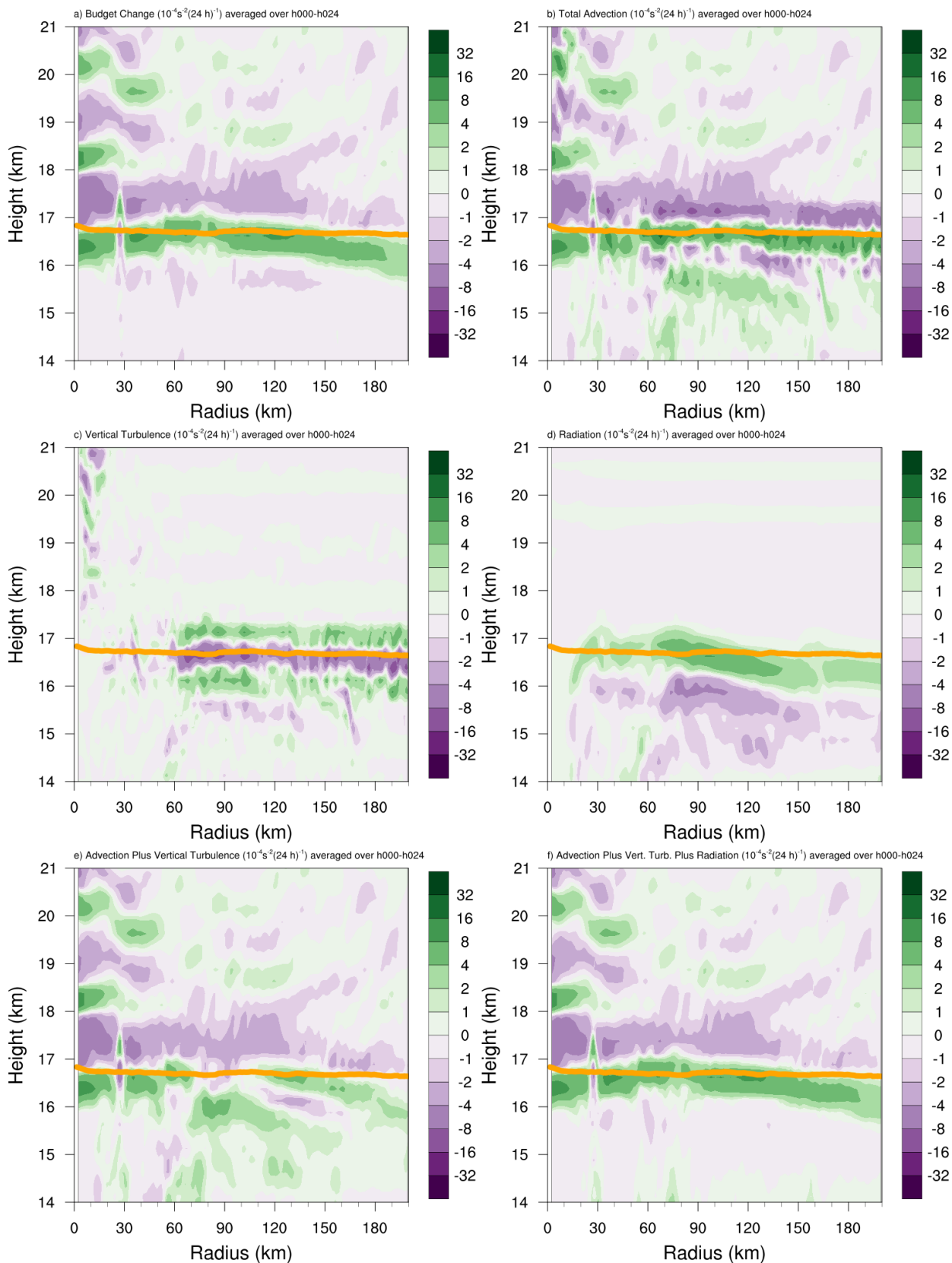


FIG. 4. Twenty-four-hour averages of squared Brunt-Väisälä frequency ( $N^2$ ;  $10^{-4} \text{ s}^{-2}$ ) over (a) 0-24 hours, (b) 24-48 hours, (c) 48-72 hours. Orange lines represent the cold-point tropopause height averaged over the same time periods.



518 FIG. 5. (a) Total change in  $N^2$  over the 0-24-hour period ( $10^{-4} \text{ s}^{-2} (24 \text{ h})^{-1}$ ) and the contributions to that change  
519 from (b) the sum of horizontal and vertical advection, (c) vertical turbulence, (d) longwave and shortwave  
520 radiation, (e) the sum of horizontal advection, vertical advection, and vertical turbulence, and (f) the sum of  
521 horizontal advection, vertical advection, vertical turbulence, and longwave and shortwave radiation. Orange  
522 lines represent the cold-point tropopause height averaged over the 0-24-hour period.

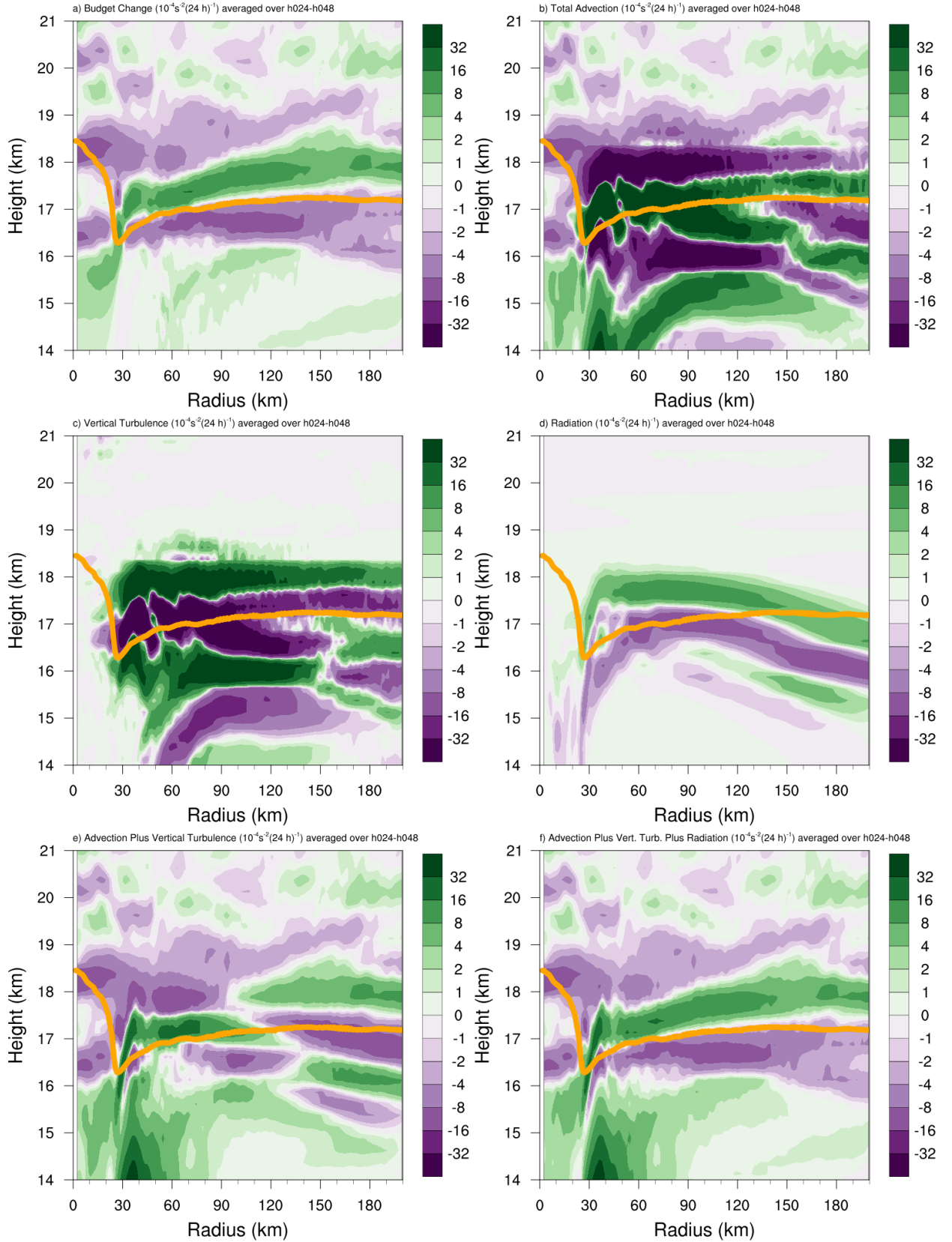


FIG. 6. As in Fig. 5, but for the 24-48-hour period.

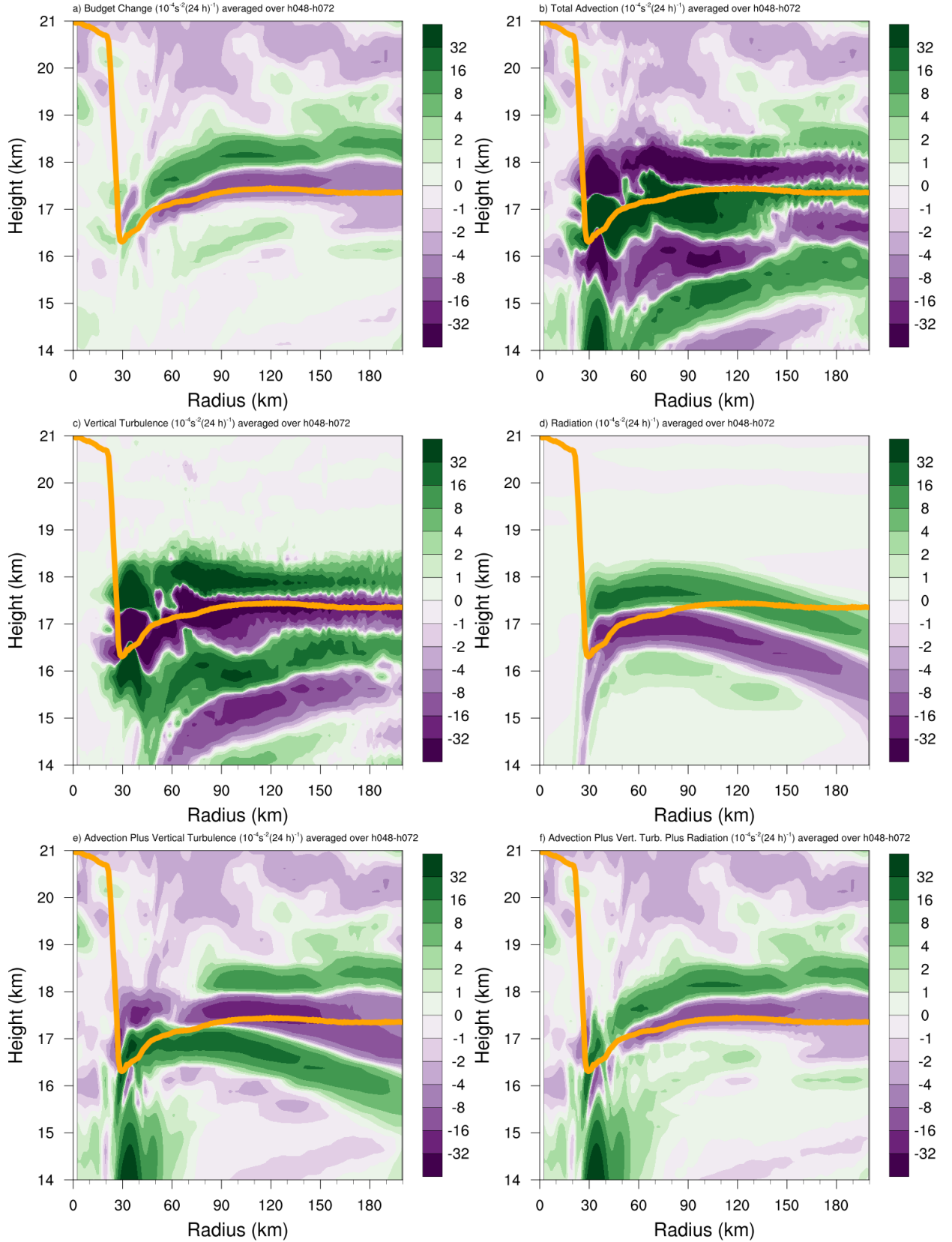


FIG. 7. As in Fig. 5, but for the 48-72-hour period.



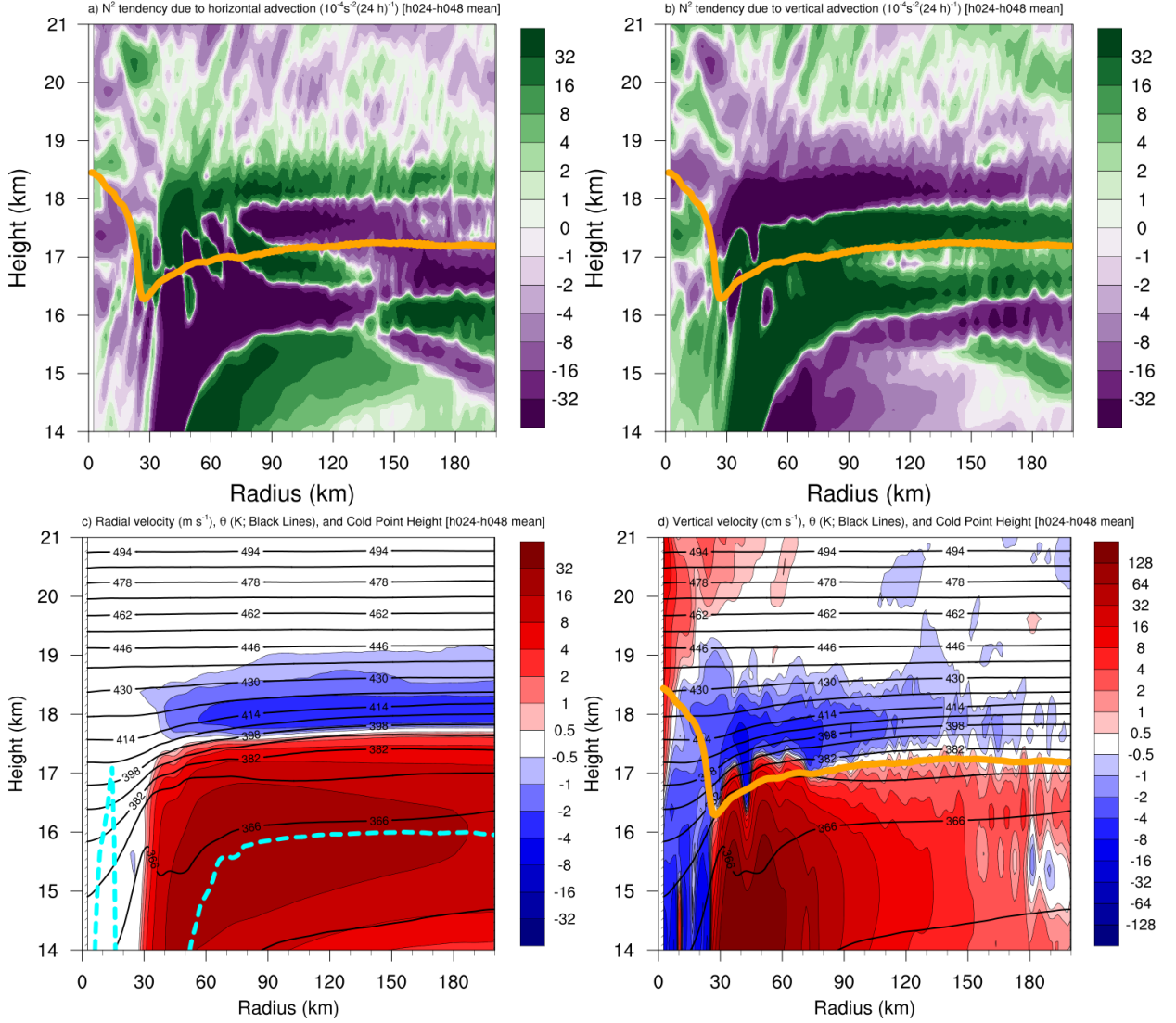
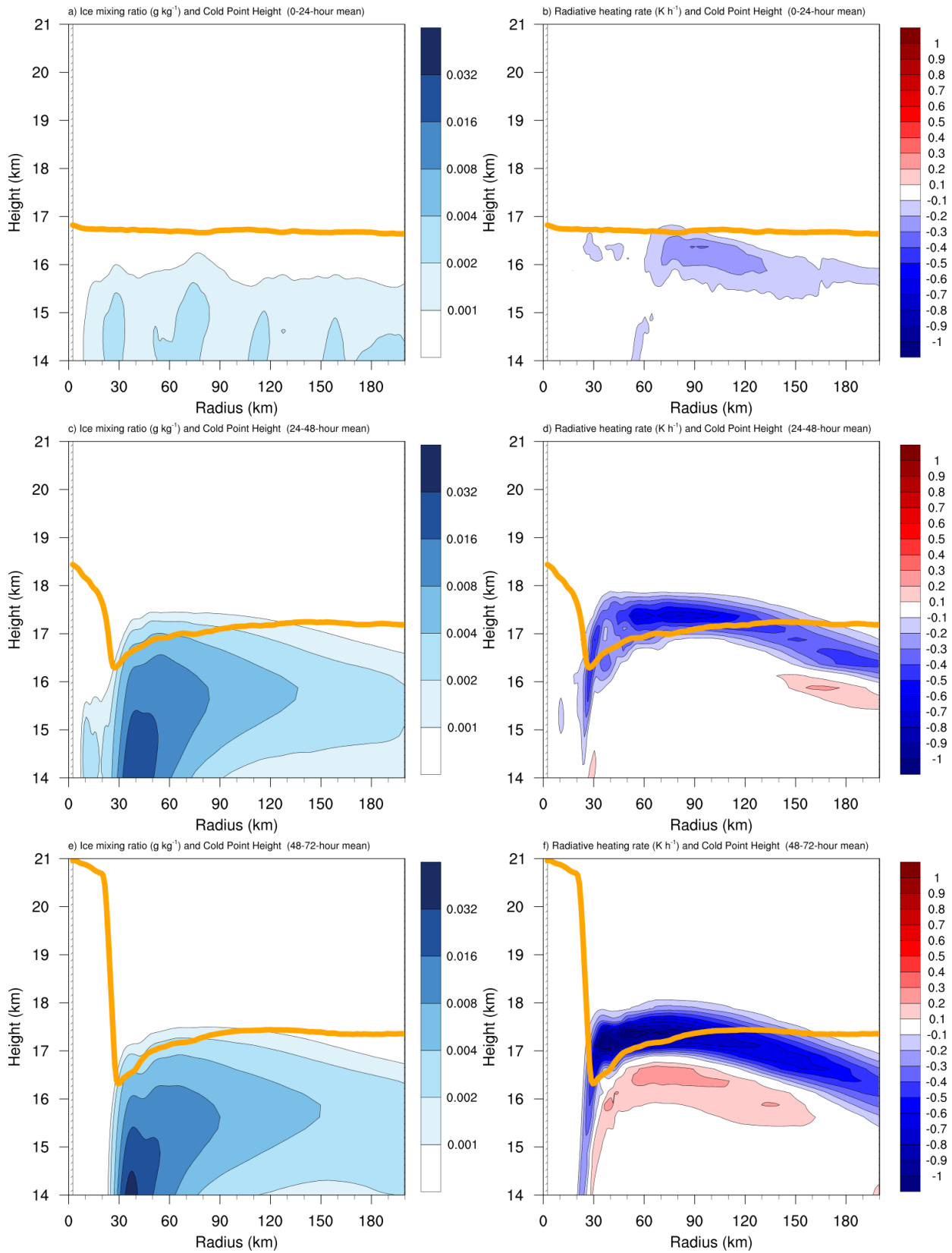


FIG. 8. The contributions to the change in  $N^2$  over the 24-48-hour period ( $10^{-4} \text{ s}^{-2} (24 \text{ h})^{-1}$ ) by (a) horizontal advection and (b) vertical advection. (c) The radial velocity ( $\text{m s}^{-1}$ ; filled contours), potential temperature (K; thick black contours), cold-point tropopause height (orange line), and level of maximum outflow (dashed cyan line) averaged over the 24-48-hour period. (d) The vertical velocity ( $\text{cm s}^{-1}$ ; filled contours), potential temperature (K; thick black contours), and cold-point tropopause height (orange line) averaged over the 24-48-hour period.



529 FIG. 9. Ice mixing ratio ( $\text{g kg}^{-1}$ ) and cold-point tropopause height (orange lines) averaged over (a) 0-24 hours,  
530 (c) 24-48 hours, and (e) 48-72 hours. Radiative heating rate ( $\text{K h}^{-1}$ ) and cold-point tropopause height (orange  
531 lines) averaged over (b) 0-24 hours, (d) 24-48 hours, and (f) 48-72 hours.

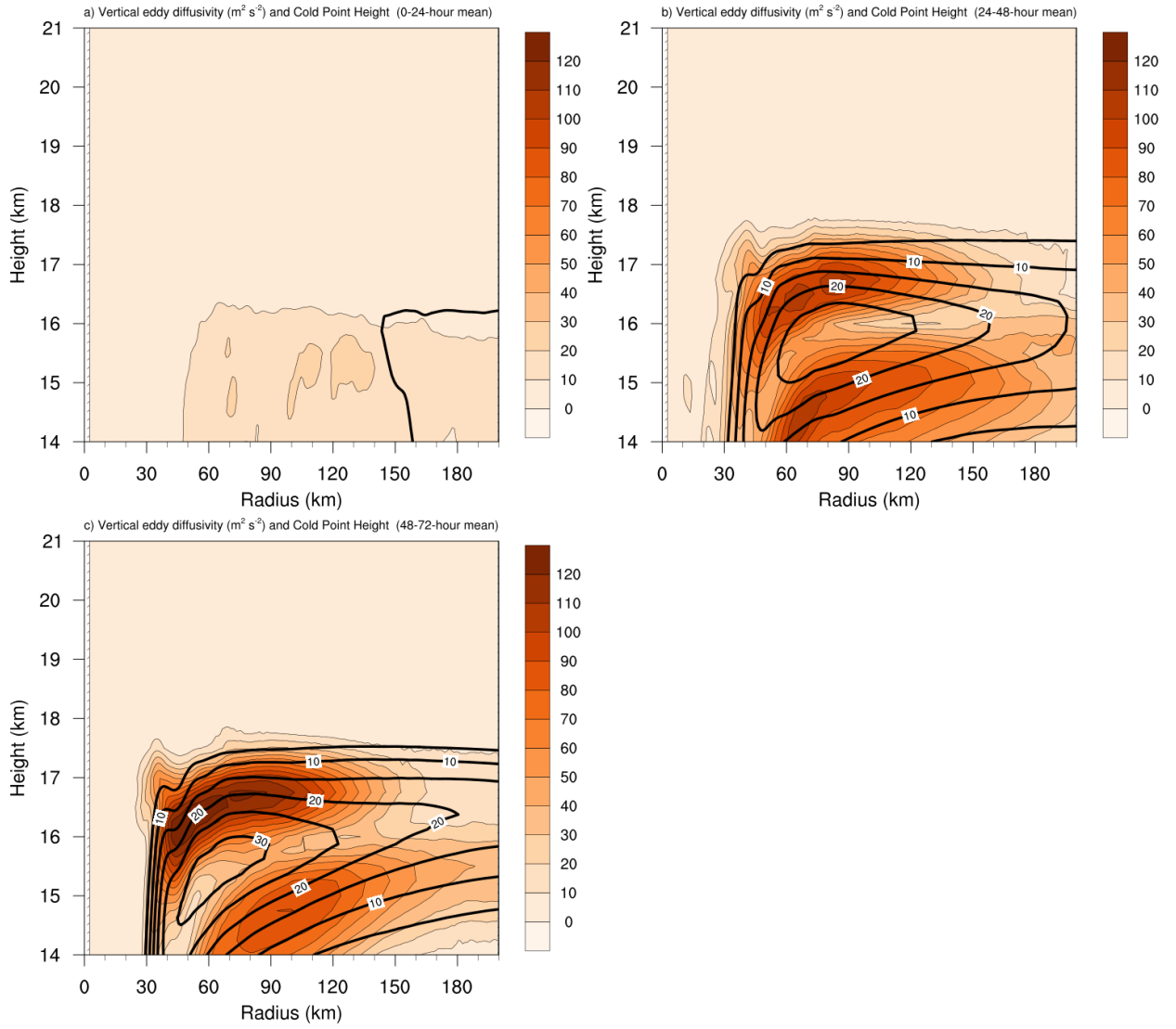


FIG. 10. Vertical eddy diffusivity ( $\text{m}^2 \text{s}^{-2}$ ; filled contours), cold-point tropopause height (cyan lines), and radial velocity ( $\text{m s}^{-1}$ ; thick black lines) averaged over (a) 0-24 hours, (b) 24-48 hours, and (c) 48-72 hours.

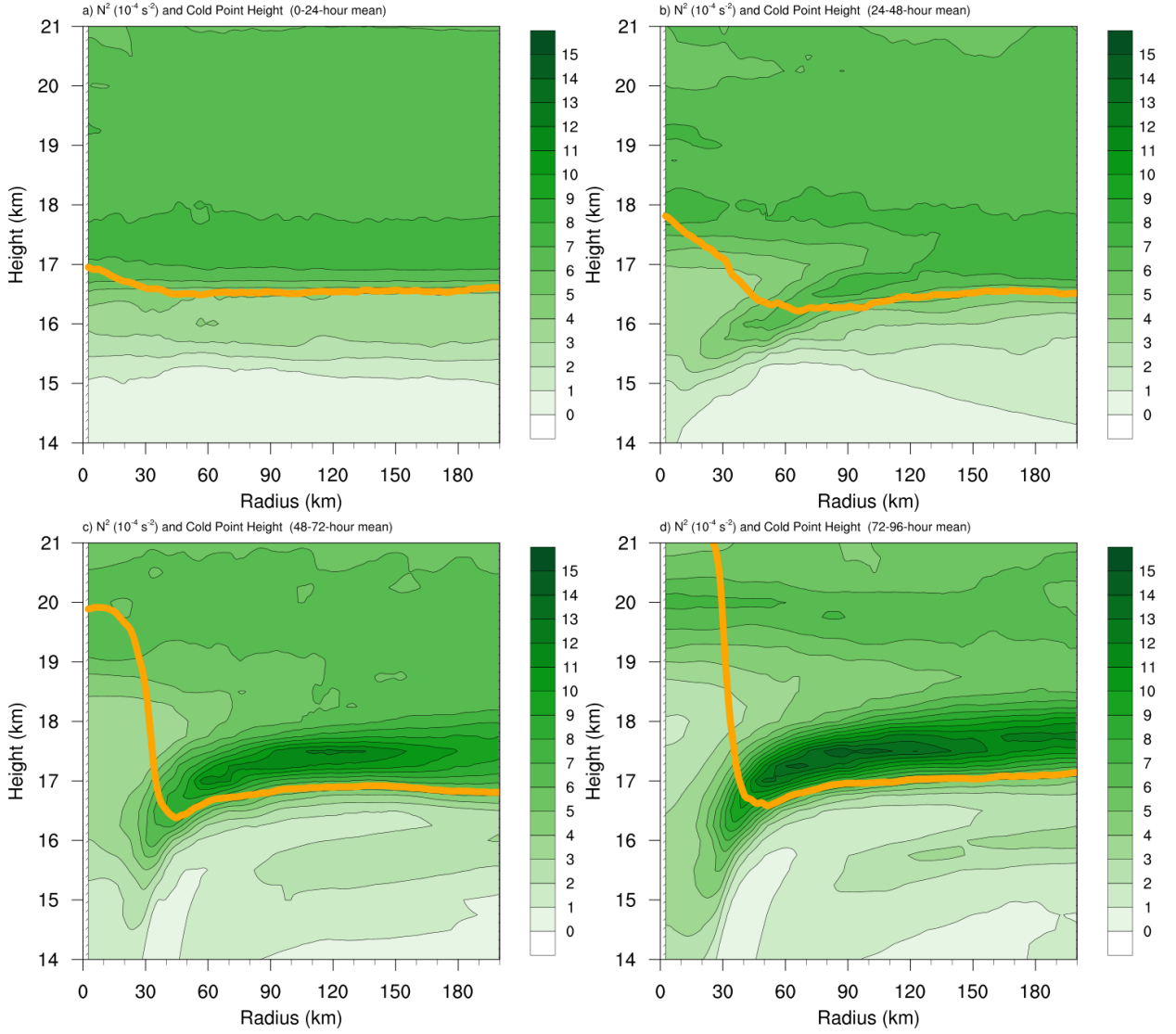


Fig. A1. Twenty-four-hour averages of squared Brunt-Väisälä frequency ( $N^2$ ;  $10^{-4} \text{ s}^{-2}$ ) over (a) 0-24 hours, (b) 24-48 hours, (c) 48-72 hours, and (d) 72-96 hours for the simulation described in Appendix Aa. Orange lines represent the cold-point tropopause height averaged over the same time periods.

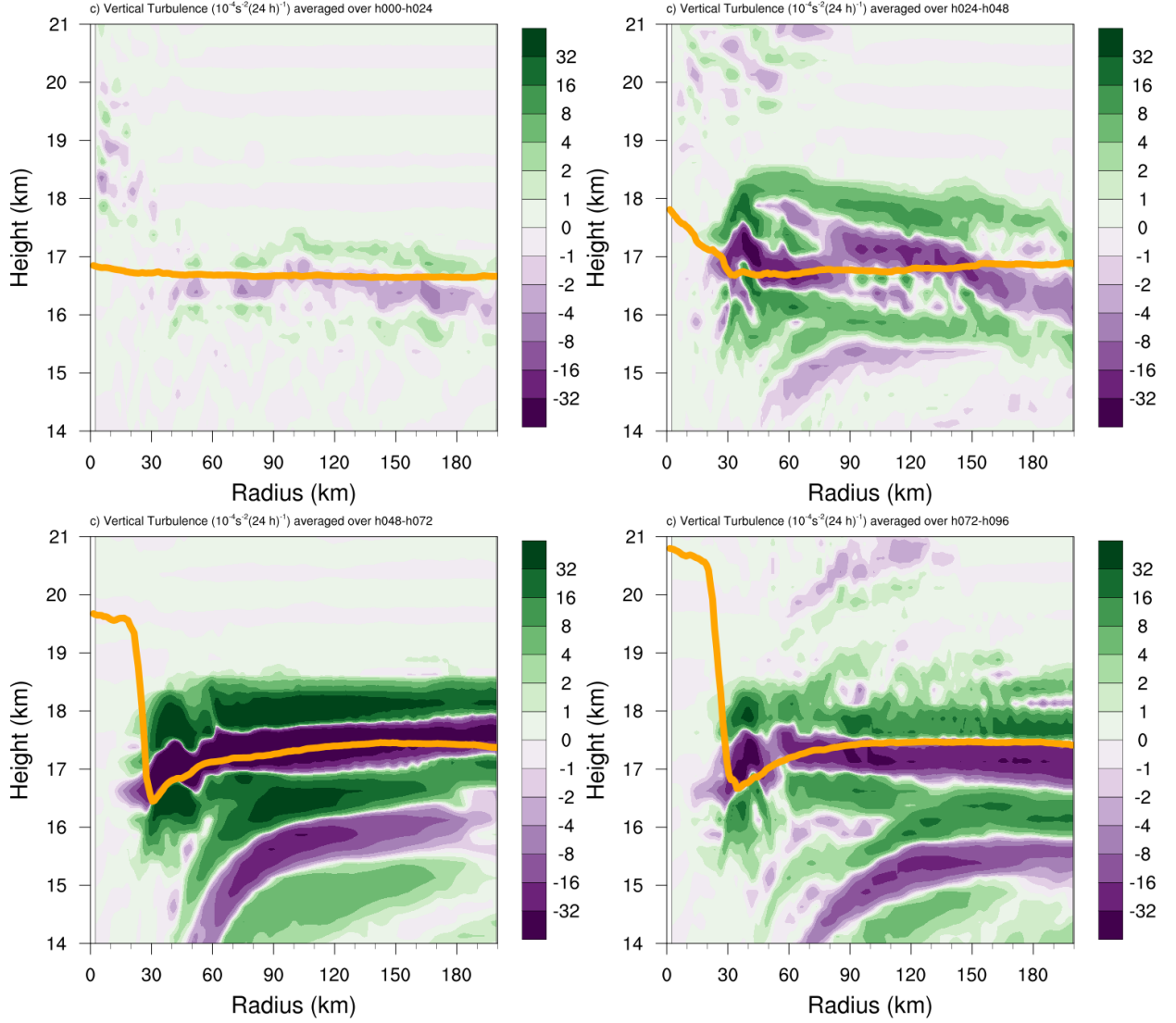


Fig. A2. The contribution of vertical turbulence to the  $N^2$  variability ( $10^{-4} \text{s}^{-2} (24 \text{ h})^{-1}$ ) averaged over (a) 0-24 hours, (b) 24-48 hours, (c) 48-72 hours, and (d) 72-96 hours for the simulation described in Appendix Ab. Orange lines represent the cold-point tropopause height averaged over the same time periods.